Available online at www.sciencedirect.com
SCIENCE DIRECT®
Acta Materialia 53 (2005) 2285–2294
Acta MATERIALIA
www.actamat-journals.com

Quantitative phase field simulation of deep cells in directional solidification of an alloy

C.W. Lan *, C.J. Shih, M.H. Lee

Department of Chemical Engineering, National Taiwan University, Taipei 10617, Taiwan, ROC

Received 3 August 2004; received in revised form 17 January 2005; accepted 25 January 2005
Available online 2 March 2005

Abstract

The formation of deep cells after the onset of Mullins–Sekerka instability during the thin-film directional solidification of a succinonitrile/acetone alloy has been simulated quantitatively by phase field modeling. The solute trapping introduced by the diffusive interface is corrected by a simple interface model, so that at the interface the equilibrium segregation is restored and the Gibbs–Thompson relation is satisfied. With the increasing pulling speed, the transitions from planar to $\lambda_c/2$ shallow cells, smaller wavelength finite-depth cells, and deep cells are clearly illustrated. The formation of deep cells with change of overall morphologies is performed, and its wavelength transition is consistent with the reported experiments. Furthermore, during the development of a cellular pattern starting from a planar interface, the crossover wavelength under different solidification speeds, where the deformation is comparable to the wavelength, agrees reasonably well with the Warren–Langer theory.

Keywords: Phase field simulation; Deep cells; Morphological instability; Directional solidification

1. Introduction

The morphological transition during alloy solidification above the onset of instability is one of the most important research topics for pattern formation in materials science and physics. The planar interface becomes unstable at a certain critical value of the control parameter, either the pulling speed (V) or the temperature gradient (G), as described by the classical Mullins–Sekerka (MS) theory [1]. This morphological instability occurs when the constitutional supercooling overcomes the stabilizing effects of the thermal gradient and interfacial tension. As observed experimentally, once the instability starts, shallow cellular structures grow initially followed by deep cells and then dendrites with the increasing speed or decreasing thermal gradients. Due to the long time and length scales of shallow cellular growth [2], most observations of the cellular morphology during thin-film solidification for transparent organic materials have shown that cells are separated by grooves so deep that a distinct bottom cannot be detected [3]. Experimental results from Eshelman et al. [4] for the solidification of a SCN/acetone alloy illustrated the morphological evolution from shallow to deep cells. They observed that in addition to the increase of the groove depth (A), the spatial wavelength (λ) of cells also changes. Especially for the transition from shallow to deep cells, the wavelength increases steeply with the increasing speed when approaching the deep cellular region. In terms of numerical solutions, Ungar and Brown [5] used mixed Cartesian and cylindrical coordinates to model deep cells, and the $\lambda_c/2$ deep cells were obtained and these structures lie on the $\lambda_c/2$ branch after shallow cells; λ_c is the critical wavelength at the onset of MS instability. However, because of the limitation of the

* Corresponding author. Tel./fax: +886 2 2363 3917.
E-mail address: cwlan@ntu.edu.tw (C.W. Lan).

1359-6454/$30.00
doi:10.1016/j.actamat.2005.01.034

front-tracking method, the wavelength transition from shallow to deep cells has not yet been reported in the previous numerical simulations. More importantly, the dramatic increase of the wavelength at the shallow/deep-cell transition has not yet been simulated.

Indeed, over the last two decades, significant progress in pattern formation during alloy solidification has come through better understanding of the fundamental aspects of interface dynamics [6]. In a typical thin-film directional solidification system, the planar interface could be stable at steady state, but become unstable during the transient build-up of the solutal boundary layer, as pointed out in the Warren–Langer (WL) theory [7]. Their analysis is based on a sudden increase of the pulling speed from a stationary planar interface to a velocity that the planar interface eventually destabilizes and evolves into a deep cellular or dendritic pattern. By analyzing the morphological stability of the planar interface during the transient, and taking into account the instability that takes time to grow from natural modulations to an observable state, an accurate prediction of the crossover wavelength λ_0 is possible [7,8]. Nevertheless, the comparison of numerical simulation and the WL theory has not yet been reported so far. After the instability, depending on the pulling velocity, the prediction of the morphology developed or the pattern formed requires a fully nonlinear simulation of the Stefan problem coupled with the mass conservation equation for solute. However, the simulation from the onset of the instability to shallow cells, deep cells, or dendrites is formidable by using the front-tracking method [5]. In fact, as just mentioned, the predicted wavelength transition from shallow to deep cells was not consistent the experimental observations.

The phase field method has emerged as a powerful tool to simulate microstructure evolution in solidification [9–11]. However, limited by computation and its inherent numerical nature, the phase field model has encountered some difficulties for realistic simulation. One of the critical limitations in the phase field simulation is on the interface thickness δ. The choice of δ needs to be small enough, so that the sharp-interface limit can be achieved. However, such a value, which is usually in the order of the microscopic capillary length d_0, is too small from the simulation point of view. This is particularly a problem for the simulation of morphological transitions during thin-film directional solidification at low pulling speeds because the time for the cells to develop is extremely long. On the other hand, at high pulling speeds, the finite thickness causes solute trapping [12]. As a result, the equilibrium behavior of the sharp interface cannot be maintained.

For the solidification of a pure substance, significant progress has been made by Karma and Rappel [13] for the thin-interface limit that δ can be chosen in the same order of the scale of microstructure. In addition, the kinetic effects can play no role on the solution. Recently, Amberg [14] has further successfully reduced the problem to the interface with a special selection of the double-well function, which can be solved analytically. The solution at the interface is equivalent to the Gibbs–Thomson equation with a special selection of the parameters allowing a thicker interface to be used. However, for the alloy phase field model, the thick interface often generates significant solute trapping which destroys thermodynamic relations at the interface [12]. To amend this, Karma [15] proposed an anti-solutal trapping scheme for a typical binary phase field model. He showed that by adding an artificial anti-trapping current to the model, the dendrite tip speed as well as the solute profile in the solid for a thin interface can be achieved by using a 'thick' interface. Although this model seems to be quite successful in some applications [16,17], the predicted solute profile in the solidification front is often not physical.

Recently, we have developed an alternative approach to restoring the local equilibrium at the interface considering the contributions of the interface thickness and solidification speed [18]. With this, a quantitative phase field simulation using a thick interface, but with a thickness still smaller than the cell tip radius, is possible even at high pulling speeds. In this report, with this approach, deep cellular transients from an initially planar interface are simulated quantitatively by the phase field method for the first time, and the results are consistent with the reported experiments. We take the directional solidification of a succinonitrile (SCN)/acetone alloy under a realistic concentration $c_0 = 0.05$ mol% and thermal gradient $G = 100$ K/cm as an example. Since the constraint of interface thickness can be greatly released, the long time/length-scale morphological transition from planar or shallow cells to deep cells with the increasing pulling speed can be clearly illustrated. In Section 2, the quantitative phase field model with the simple interface modification is described briefly. Section 3 is devoted to results and discussion, followed by conclusions in Section 4.

2. Quantitative phase field model for dilute alloys

In the phase field model, the directional solidification of a binary alloy containing components A (solvent) and B (solute) in a given thermal profile is described by a phase field variable $\phi(x,y,t)$ and concentration $c(x,y,t)$. Assuming the values $\phi = 0$ in the solid and $\phi = 1$ in the melt, the variation of this variable can be defined as a hyperbolic function in the normal coordinate n changes rapidly from 0 to 1 at the interface:

$$\phi = \frac{1}{2}\left[1 + \tanh\left(\frac{n}{2\delta}\right)\right]. \quad (1)$$

Following the geometrical formulation proposed by Beckermann et al. [19], one can define the unit normal vector $\mathbf{n}$, the local curvature κ, and the interface speed V_n as

$$\mathbf{n} = \frac{\nabla\phi}{|\nabla\phi|},$$
$$\kappa = \nabla\cdot\mathbf{n} = \frac{1}{|\nabla\phi|}\left(\nabla^2\phi - \frac{\nabla\phi\nabla|\nabla\phi|}{|\nabla\phi|}\right), \quad \text{and}$$
$$V_n = \frac{-1}{|\nabla\phi|}\frac{\partial\phi}{\partial t}.$$

By substituting them into the generalized Gibbs–Thompson (G–T) equation (for a dilute alloy having an isotropic surface energy σ_A), i.e.,

$$T_i = T_m^{\mathrm{A}}\left(1+\kappa\frac{\sigma_A}{L}\right) + mc_{\mathrm{L}} - \frac{V_n}{\mu_A}, \tag{2}$$

a phase field equation is obtained as the following:

$$\frac{\partial\phi}{\partial t} = \frac{\sigma_A T_m^{\mathrm{A}}\mu_A}{L_A}\left[\nabla^2\phi - \frac{\phi(1-\phi)(1-2\phi)}{\delta^2}\right] - \mu_A(T_m^{\mathrm{A}} - T + mc_{\mathrm{L}})\left[\frac{\phi(1-\phi)}{\delta}\right], \tag{3}$$

where L_A is the heat of fusion, μ_A the kinetic coefficient, and m the slope of liquidus temperature line (T_i); T_m^{A} is the melting point of pure A and c_{L} the concentration of the solute B at the liquid phase side.

Compared with previous phase field models derived from non-equilibrium thermodynamics, this model can be viewed as an intermediate between them and the classical sharp interface model. Since the realistic equilibrium conditions k and m are involved directly, additional coupling with the molecular thermodynamic model is not required. Besides, the last term in Eq. (3) indicates that one can perform quantitative simulations once the local liquid concentrations are correct. In fact, if $\frac{\phi(1-\phi)}{\delta}$ is replaced by $5\frac{\phi^2(1-\phi)^2}{\delta}$, it could be easily shown that the model is equivalent to the Karma's model [15].

For a simulation in a large domain covering the overall cell morphology and the solutal boundary layer, a thick interface thickness is preferred to reduce computational load. However, solute trapping is introduced due to the diffusive nature of the thick interface. To suppress this effect, a simple interface model is considered in this report. This model starts from the introduction of an artificial segregation coefficient k_{a}, such that $c_{\mathrm{S}}/c_{\mathrm{L}} = k_{\mathrm{a}}$ in the diffusive interface, where the solute concentrations in the liquid (c_{L}) and the solid (c_{S}) can be related to the average concentration c as:

$$c_{\mathrm{L}} = \frac{c}{p(\phi) + k_{\mathrm{a}}(1-p(\phi))} \quad \text{and}$$
$$c_{\mathrm{S}} = \frac{k_{\mathrm{a}}c}{p(\phi) + k_{\mathrm{a}}(1-p(\phi))}, \tag{4}$$

respectively. Here, $p(\phi)$ is an interpolation function to describe solid–melt mixture properties. The concentration equation can also be derived based on the conservation of solute as

$$\frac{\partial c}{\partial t} = \nabla\cdot[(1-p(\phi))D_{\mathrm{S}}\nabla c_{\mathrm{S}} + p(\phi)D_{\mathrm{L}}\nabla c_{\mathrm{L}}]. \tag{5}$$

For comparison purposes, the weighting function $p(\phi)$ between melt and solid is taken directly from the WBM model [2], where $p'(\phi) = 30g(\phi)$; $g(\phi) = \phi^2(1-\phi)^2$ is a double-well function. By selecting different functions, this model can be rearranged to other phase field models [9,19].

Because the interface is finite and diffusive, k_{a} is not same as the equilibrium one (k), but is affected by the interface thickness and the interface speed, unless the interface thickness is very near the sharp interface limit. In other words, with a thick interface the calculated partition, or the effective segregation coefficient $k_{\mathrm{eff}} = c_{\mathrm{S}}/c_{\mathrm{L}}$, obtained by a typical phase field model, is greater than the equilibrium k if $k < 1$; c_{S} and c_{L} are the concentrations defined at the solid ($\phi < 0.1$) and liquid ($\phi > 0.9$) sides of the interface, respectively. It should be pointed out that the weight function p changes rapidly with ϕ. At $\phi = 0.9$, the p function is higher than 0.99; similarly, at $\phi = 0.1$, the p function is less than 0.01. In other words, the highest concentration is right at the melt edge of the interface, which is the value we pick for calculation; the solid side is similar. Therefore, if one can find an interface model for the thick diffusive interface such that $k_{\mathrm{eff}}(\delta, V_n, k_{\mathrm{a}}) = k$ locally, and the calculated result at the interface can also satisfy the G–T equation, a quantitative phase field simulation at any δ and V_n is possible without the apparent solute trapping. On the other hand, since the interface (boundary) conditions for concentration and temperature are correct, their profiles in the melt and solid can be calculated accurately as well. Now the next question is to find a simple relation for the calculated partition k_{eff} (obtained from the concentration across the interface) as a function of the interface speed and thickness. Moreover, the concentration partition across the interface is about the same as $c_{\mathrm{S}}/c_{\mathrm{L}}$ at the interface by using the extrapolated concentration from the solid and liquid sides if the solute boundary layer thickness is much larger than the interface thickness. Then, having $k_{\mathrm{eff}} = k$, we can find the value of k_{a}, and the interface model should be able to obtain this value.

The simple interface model is developed by considering the correlation of the effective segregation coefficient k_{eff}, the interface diffusion speed V_{D}, and the thickness δ as:

$$V_{\mathrm{D}} = a\frac{D_{\mathrm{L}}\ln(1/k_{\mathrm{a}})}{\delta(1-k_{\mathrm{a}})}, \tag{6}$$

where a is a free parameter. This formulation is very similar to the one proposed by Aziz and Kaplan [20] and Ahmad et al. [12], but the free parameter a needs

to be determined. In addition, we can further correlate V_D with V_n similar to that in Refs. [12,20] by

$$k_{\text{eff}} = (k_a + V_n/V_D)/(1 + V_n/V_D). \tag{7}$$

By substituting V_D in Eq. (6) into Eq. (7), $k_{\text{eff}}(\delta, V_n, k_a)$ is obtained. Again, here $k_{\text{eff}} = c_S/c_L$ is the solute partition across the interface. Then, the simple interface model is simply to let $k_{\text{eff}} = k$, i.e., $c_S/c_L = k$, to restore the correct solute partition at the interface; c_S and c_L are obtained by the phase field calculation for given δ, V_n, and k_a.

When δ and V_n are given, giving a and k_a to obtain $c_S/c_L = k$ has no unique solutions, i.e., one equation (Eq. (7)) with two unknowns. However, with some simple and easy calculations, a best fit value can be found; once an optimum a is determined, k_a can be calculated from Eqs. (6) and (7). Furthermore, if the interface thickness δ is much smaller than the tip radius, this local model is purely one dimensional (1D) and is independent of the convection away from the interface. If so, 1D calculations serve the best way of finding the best value of a. Through a few 1D simulations (planar interface), which are very easy to do, a best-fit value of $a = 0.56$ is found. In other words, with various δ and speed V_n, we can extract c_S and c_L from the interface having a correct partition, i.e., $c_S/c_L \sim k$, where the solute trapping effect is almost removed. This model can be easily used during simulation because the value of V_n can be easily calculated locally. More importantly, we also find that the Gibbs–Thompson relation is satisfied nicely, where the corrected concentration is the most important factor here. Furthermore, this model is extended to a much wider range of pulling speeds and interface thicknesses over two orders, and no apparent solute trapping is found. The only constraint for δ is that the interface thickness needs to be smaller than the local tip radius ρ [14,17]. The detailed numerical test of this model can be found elsewhere [18].

For directional solidification, Eqs. (3) and (5) are represented in a moving frame at a stable pulling speed V. The inlet or the far field concentration is c_0, while the outlet boundary condition is set by zero derivatives in the pulling direction. The effect of anisotropy is considered in the same manner as in the previous models [16,17,19]. In order to present the governing equations in dimensionless form, the variables are rescaled. The solute concentration (atomic fraction) c is rescaled by c_0 to c^*. The dimensionless temperature is defined by $\theta = \frac{(T-T_L)}{\Delta T}$, where T_L is the temperature at the lower boundary and $\Delta T = T_H - T_L$ is the temperature difference between the hot zone (T_H) and the cold zone (T_L). The length, in terms of the coordinates x and y, is rescaled by l to x^* and y^*, respectively, and time t by l^2/D_L to t^*, where l is a characteristic length and l^2/D_L is a characteristic time; D_L is the solute diffusivity in the liquid. The phase field variable ϕ is set to be 1 in liquid and 0 in solid, while 0.5 at the interface. The steady frame moving speed V is rescaled by D_L/l to V^*. Then, the dimensionless governing equations are written as the following:

$$\begin{aligned}\frac{\partial\phi}{\partial t^*} - V^*\frac{\partial\phi}{\partial y^*} &= M^*\left[\nabla\cdot(\eta^2\nabla\phi) - \frac{\partial}{\partial x^*}\left(\eta\eta_\beta\frac{\partial\phi}{\partial y^*}\right) + \frac{\partial}{\partial y^*}\left(\eta\eta_\beta\frac{\partial\phi}{\partial x^*}\right)\right] \\ &\quad - M^*\left[\frac{l^2}{\delta^2}\phi(1-\phi)(1-2\phi)\right] \\ &\quad - \frac{l^2\mu_A}{D_L}\left[\Delta T(\theta_m^A - \theta) + mc_0c_L^*\right]\frac{\phi(1-\phi)}{\delta},\end{aligned} \tag{8}$$

$$\frac{\partial c^*}{\partial t^*} - V^*\frac{\partial c^*}{\partial y^*} = \nabla\cdot\tilde{D}^*\left[\nabla c^* - \frac{(1-k_a)p'(\phi)c^*}{p(\phi)+k_a[1-p(\phi)]}\nabla\phi\right], \tag{9}$$

where

$$c_L^* = \frac{c/c_0}{p(\phi)+k_a(1-p(\phi))},$$

$$\tilde{D}^* = \tilde{D}/D_L, \quad \text{and} \quad \tilde{D} = D_S + \frac{[p(\phi)(D_L - D_S)]}{[p(\phi)+k_a(1-p(\phi))]},$$

D_S is the solute diffusivity in the solid phase. In addition, the dimensionless mobility $M^* = M/D_L = \frac{\mu_A\sigma_A T_m^A}{D_L L_A}$ can then be defined. Furthermore, the anisotropic function η in Eq. (8) is defined for the fourfold symmetry [11], i.e., $\eta = 1 + \gamma\cos 4\beta$, where γ is the intensity of the anisotropy (0.04 is used), and $\beta = \tan^{-1}[(\partial\phi/\partial y)/(\partial\phi/\partial x)]$ determining the growth orientation of the cells. In this study, we have purposely chosen (1 0 0) in the x-direction and (0 1 0) in the y-direction. Also, to balance the realistic modeling and computational effort, the kinetic coefficient μ_A is tuned as large as possible so that the kinetic effect can be neglected. As pointed out previously, when $\frac{\phi(1-\phi)}{\delta}$ is replaced by $5\frac{\phi^2(1-\phi)^2}{\delta}$, the phase field model is equivalent to Karma's model [19]. Based on Karma's thin-interface model, the kinetic coefficient can be determined as the following:

$$\frac{1}{\mu_k} = [5a_2/4][\delta/D_L][(D_L L/\alpha C_p) - m(1-k)c], \tag{10}$$

where $a_2 = 0.6267$ [17], α the thermal diffusivity, and C_p the heat capacity. With this equation, the kinetic coefficient is about 0.01 m/K s; the value is smaller as the concentration effect is considered. In fact, we have observed that the value greater than 0.002 gives about the same result. More interestingly, the use of $5\frac{\phi^2(1-\phi)^2}{\delta}$ does not much affect the result, but it seems to be more robust in the simulation; the timestep could be larger. Where the value is greater than 0.01 m/K s, the timestep needs to be smaller for numerical stability. This kinetic coeffi-

cient contributes the temperature difference in the G–T equation, depending on the velocity, is less than 0.02 K. In addition, with a careful selection of the parameters and interpolation functions, the WBM model used in our previous report [16] could be reduced to Eq. (8) for the pure material [9]. Moreover, the major difference between our model and Karma's anti-trapping model is in the treatment of the solute equation (Eq. (9)). We use the simple interface model to get the apparent k_a, instead of introducing an anti-trapping current. The physical meaning of both models should be the same once interface thickness and speed are taken into account. In Karma's approach, the anti-trapping current is used to pump back the solute to reduce the partition (increasing c_L). On the other hand, our model predicts k_a to be smaller than k (for $k < 1$), while the simulated segregation k_{eff} could be equal to k. Both approaches attempt to get the right partition, i.e., thermodynamic consistency. In addition, since the interface thickness is usually thin as compared with the heat and solute boundary layers, once the partition is right, i.e., having a correct interface condition, the solute transport in the melt ($\phi = 1$) and the solid ($\phi = 1$) could be calculated correctly. The numerical implementation of the present model is simpler than that of Karma's model. However, a few 1D calculations for getting the parameter a by linear regression are necessary here.

The simulation is performed for SCN with 0.05 mol% acetone at a thermal gradient of 100 K/cm. A computational domain with a large computational domain is considered to accommodate the long solutal boundary layer, and the frozen temperature approximation (FTA) having a constant thermal gradient G is adopted by neglecting the latent heat as a working assumption. This assumption has also been checked by non-FTA calculations, and the morphological dynamics, except the absolute position, are almost not affected. This moving-frame system can be regarded as a domain having a steady material flow coming in from the top and out from the bottom, as sketched in Fig. 1(a), where a portion of the domain (300×1000 μm^2) is presented. Therefore, at the top boundary, the concentration is specified ($c^* = 1$), while at the lower boundary the exit condition is used, i.e., $\partial c^*/\partial y^* = 0$. On both sides of the domain, the symmetry (no flux) condition is used ($\partial\phi/\partial x^* = 0$, $\partial c^*/\partial x^* = 0$). A thick interface thickness $\delta = 0.5$ μm is used to balance the computational load and local numerical resolution. Eqs. (8) and (9) with a given initially planar condition (liquid concentration $c_L^* = 1$, solid concentration $c_s^* = 0.1$, and interface temperature $T_i = 331.122$ K) can then be solved by an adaptive finite volume method [21], where the minimum grid size (Δx) is smaller than the interface thickness δ. A sample of the adaptive mesh is sketched in Fig. 1(b). During calculation, the mesh is adaptively refined and coarsened along the interface and high concentration-gradient regions. The maximum number of finite volumes is about 100,000 depending on the complexity of the morphology, and all the calculations are performed efficiently in a personal computer (Pentium-4 3G CPU with 512 Mbyte DDR RAM).

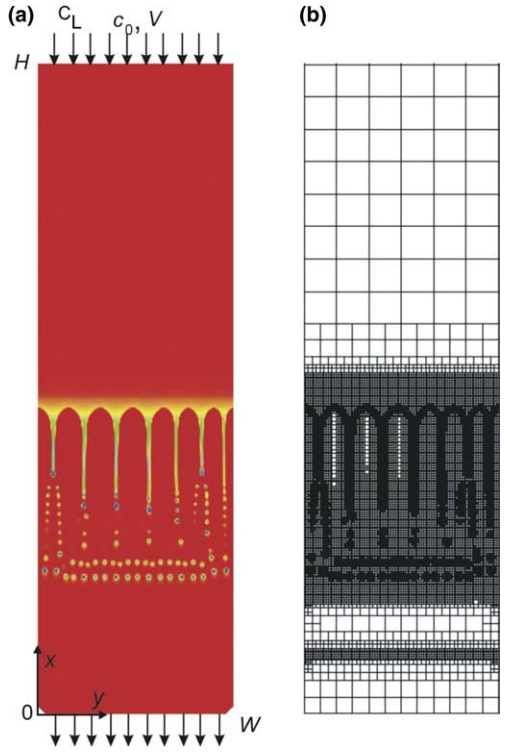

Fig. 1. (a) Schematic of the computational domain for the phase field modeling of thin-film directional solidification in a moving frame with a speed V; (b) a sample adaptive finite volume mesh.

3. Results and discussions

3.1. Deep cellular structures

In the classical MS theory [1], under a known thermal gradient, the planar interface becomes unstable and wrinkled at a wavelength λ when the pulling speed is larger than the critical speed. In the present simulation, the lowest critical speed V_c is 13.21 μm/s, which corresponds to the critical wavelength λ_c at 135 μm. To verify the quantitative simulation, the steady-state morphologies from planar to shallow cellular interfaces with the increasing pulling speed are highlighted in Fig. 2. For all speeds, the simulated solute profile on the liquid side of the solidification front is an exponential decay function, and is in good agreement with the exact solution. In addition, the calculated effective segregation is very close to the equilibrium one (error<1%), and is independent of the pulling speed. As shown in Fig. 2, the critical speed simulated by the phase field model lies between 13 and 13.5 μm/s, which also shows good agreement with the one predicted from the MS theory (13.21 μm/s). Be-

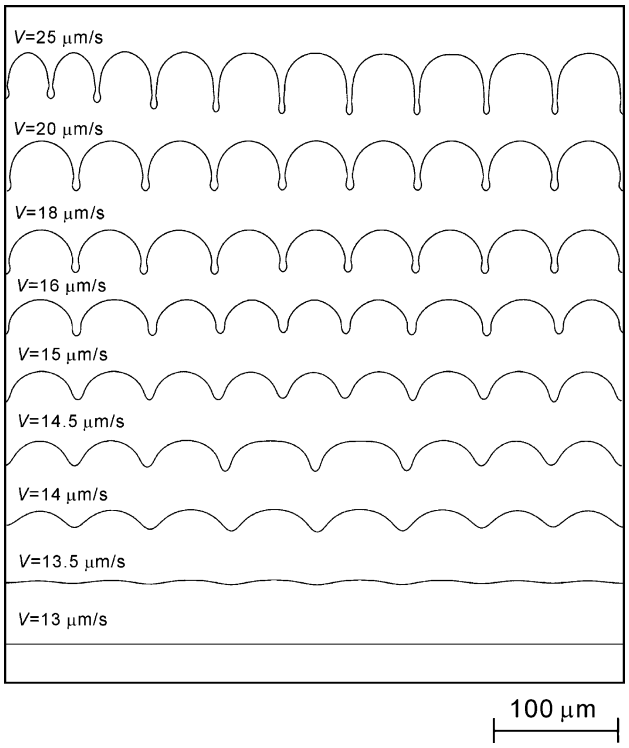

Fig. 2. Simulated morphological transition from a planar interface to the shallow cells of $\lambda_c/2$ with the increasing pulling speed V.

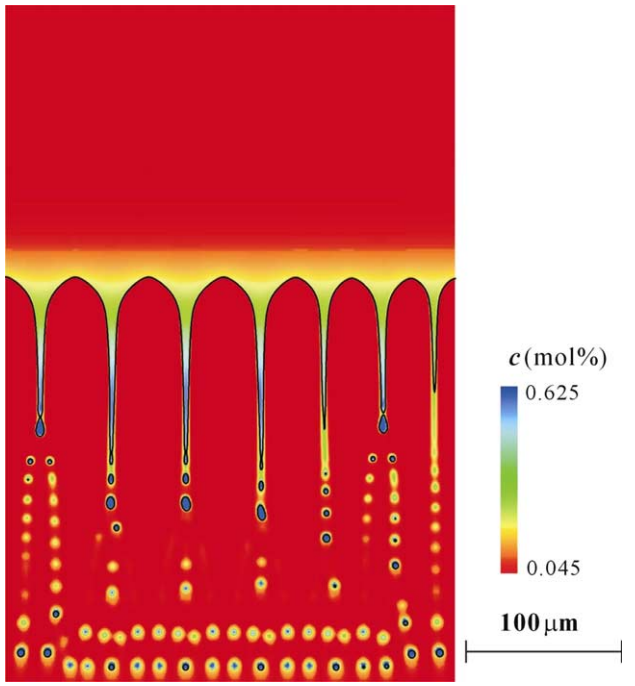

Fig. 3. A simulated deep cells and its concentration distribution (c_0 = 0.05 mol%, G = 100 K/cm, and V = 80 μm/s).

sides, the spatial wavelengths are about 55.6–62.5 μm, and they lie on the bifurcation branch of $\lambda_c/2$ [2]. For the pulling speed near the onset of instability, the solidification speed is relatively small, and is much smaller than the value of V_D here. Accordingly, the effect of non-equilibrium is small. In other words, once the solute distribution near the interface is correct, a good prediction of the amount of the constitutional supercooling can be easily obtained.

In real experiments, the structure of deep cells may emerge when the pulling speed is about five times that of the critical one [4,22,23]. Due to the relatively higher solidification speed, solutal trapping is found to be important for the current interface thickness (δ = 0.5 μm). Therefore, to amend this problem, using the simple interface model mentioned previously, is necessary. Starting from a suitable initially planar condition, the morphologies under different pulling speeds are performed similarly. A sample of simulated deep cellular structure and solute distribution is plotted in Fig. 3. As shown, the deep cells are quite similar to the ones obtained in the previous experiments [23], but a CBr_3/Br_2 alloy was used in Ref. [23]. However, because the interface thickness is finite, which is comparable to the distance between two cells at the bottom of grooves, the cell closures there cannot be resolved clearly. Interestingly, there are many solute drops caught randomly inside the solid phase during the fast freezing. This was also frequently observed in real experiments.

In terms of quantitative simulations, satisfying the local Gibbs–Thompson condition is very important. To verify this point, we have extracted local concentration distribution, tip radius ρ, and interface temperature T_i of a single tip under various pulling speeds. An example at V = 80 μm/s is sketched in Fig. 4, where the local tip radius is obtained by using 4th order polynomial fitting within the 3 μm domain around the tip. At this velocity, the calculated interface temperature is 330.847 K, while the one obtained from the classical Gibbs–Thompson equation is 330.915 K, without considering the kinetic effect. The deviation (0.07 K) is quite small comparing with the temperature difference ΔT = 15 K in the overall simulation domain. This deviation (<0.5%) should be small because the convergence criterion is only 0.1%. Besides, the solid and liquid concentrations are 0.0154 and 0.1542 mol%, respectively, indicating that the simulated effective segregation is also very close to the equilibrium one (k = 0.1). However, because the capillary supercooling resulting from the surface tension effect is relatively small (i.e., $T_m^A \kappa \frac{\sigma_A}{L}$ in Eq. (2) ~0.02 K) for our simulated cases, it is difficult to clarify the accuracy of interface temperature. The correctness of the curvature contribution is hard to evaluate due to the numerical limit. We have also used different kinetic coefficients ranging from 0.002 to 0.01, but the effect on the curvature is very small. Since the temperature variation across the interface is only 0.005 K, the good agreement with the G–T equation is attributed to the correct concentration calculated, because the contribution of the concentration

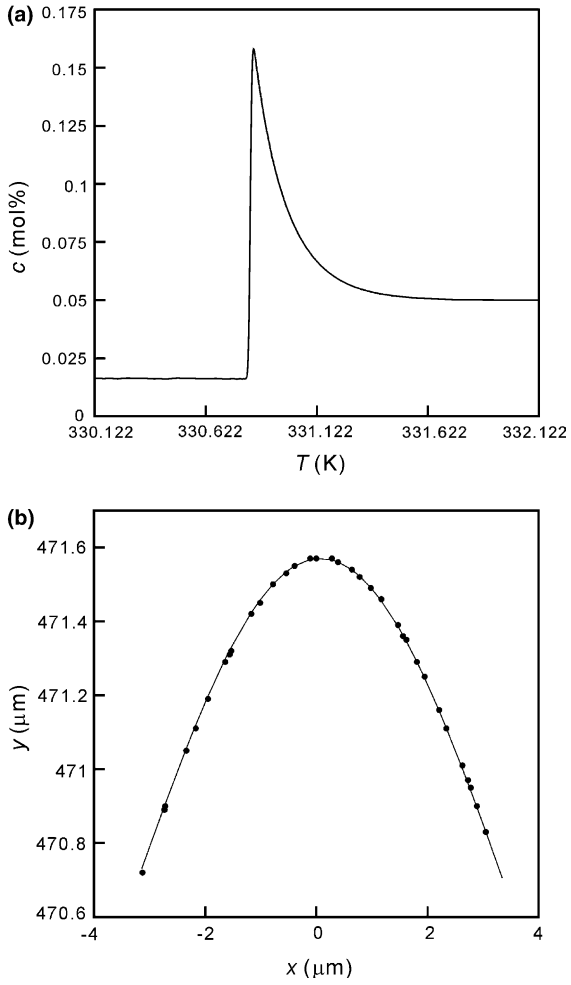

Fig. 4. Calculated (a) concentration distribution and (b) local tip radius of a deep cell under $V = 80$ μm/s.

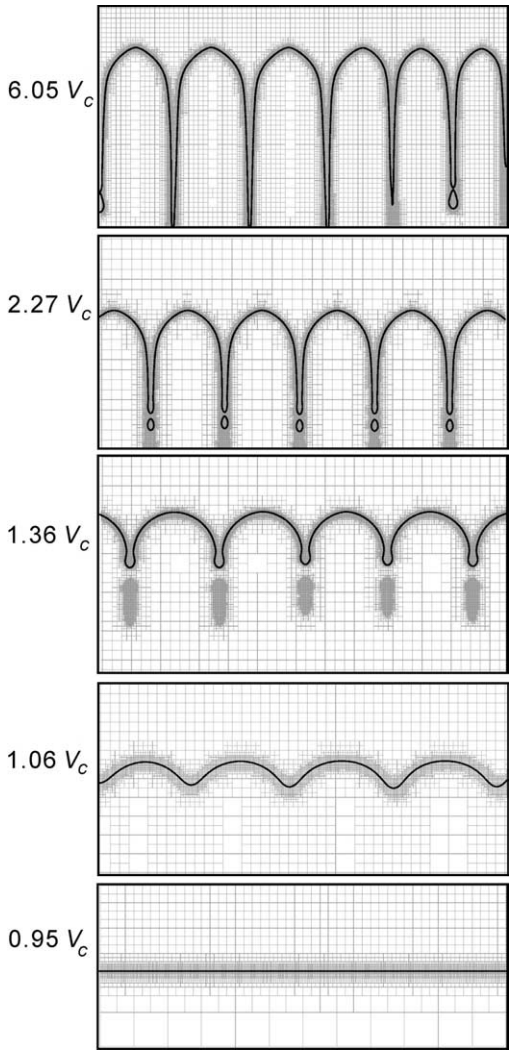

Fig. 5. Simulated cell morphologies for different pulling velocities. The adaptive finite volume mesh used in the simulation for each calculation is also illustrated.

on the interface temperature is much larger than the curvature effect. Nevertheless, the critical speed predicted by our model lies between 13 and 13.5 μm/s, which is in good agreement with the one from the MS theory. Therefore, our simulation should be reasonably accurate. The reasonable agreement with WL theory, which will be discussed shortly, also supports this model. Although the phase field model proposed here is simple and straightforward, a quantitative simulation of alloy solidification could be carried out successfully, even under high pulling speeds having a thick interface thickness.

As for cellular shapes, the simulated ones under different relative velocities are highlighted in Fig. 5, while the adaptive meshes are also plotted. As shown, the cells become deeper and their tips sharper with the increasing pulling speed, and this is consistent with experimental observations [22,23]. Besides, it is clear that the spatial wavelength indeed changes during the morphological transition. To further study the change of wavelength, amplitude, and tip radius during the transition from shallow cells to deep cells, these dimensional cell characteristics are measured as a function of the solidification speed in a log–log scale, as plotted in Figs. 6–8, respectively. As shown, three different regions can be identified. First, from the bifurcation of the planar interface ($V_c = 13.21$ μm/s) to $\lambda_c/2$ shallow cells, the wavelength is about constant, which is on the $\lambda_c/2$ branch. The amplitude increases with velocity monotonically. As the region of finite-depth cells with smaller wavelengths is approached, the increase of the amplitude slows down. In addition, the tip radius increases rapidly with the pulling speed because it is close to proceed to tip-splitting.

The finite-depth cells having smaller wavelengths appear following $\lambda_c/2$ shallow cells when the speed is higher than 22 μm/s. It is a cellular region whose wavelength decreases with velocity roughly as $V^{-1/2}$. The groove

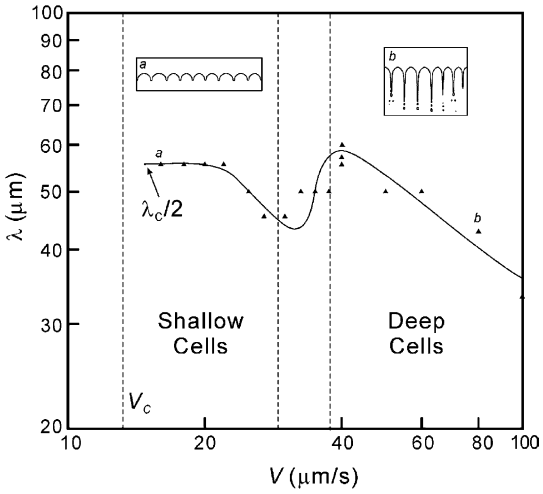

Fig. 6. Variation of the simulated wavelength λ with the pulling speed V.

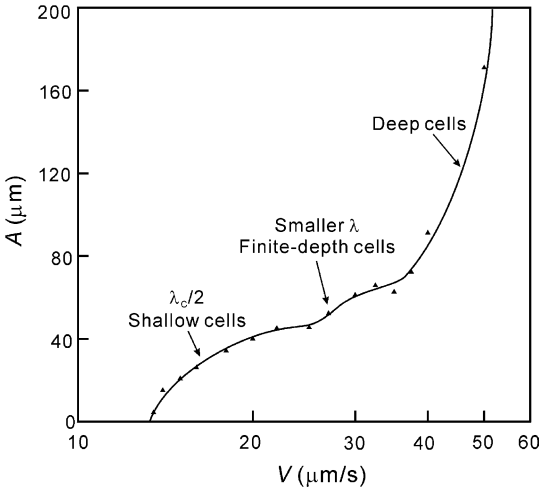

Fig. 7. Variation of the simulated groove amplitude A with the pulling speed V.

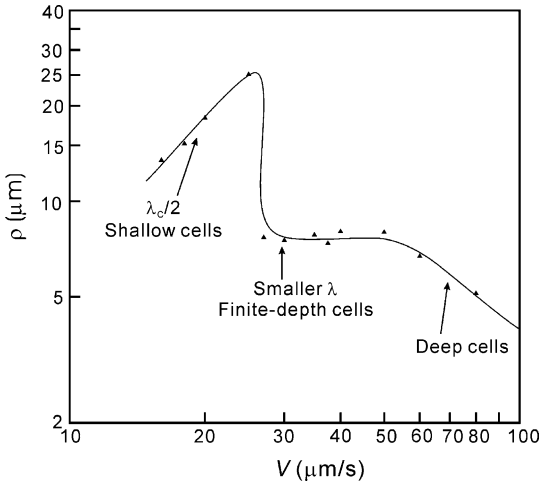

Fig. 8. Variation of the simulated tip radius ρ with the pulling speed V.

amplitude also increases with the velocity, which shows a distinct behavior from the one observed in the previous region. As the tip-splitting mechanism occurs, the overall morphology is rearranged and the tip radius decreases immediately. In this region, the variation of tip radius is almost independent of the pulling speed, which is quite different from the one for the wavelength. Beyond this region, $V\lambda^2$ is about constant for the pulling speed less than 30 μm/s.

As the groove becomes deeper and deeper, the wavelength variation is becoming more interesting. As shown in Fig. 6, there is a transition zone between shallow cells and deep cells, in which the wavelength increases with the pulling speed. This happens to be consistent with the previous experimental observations [4]. In the present study, this range lies between 30 and 40 μm/s and the local tip radius remains approximately constant. As the deep cellular structure is developed ($V > 50$ μm/s), the wavelength again decreases with the pulling speed, which is also close to $V^{-1/2}$, while the amplitude starts to increase dramatically (Fig. 7). The local tip radius in Fig. 8 also shows a similar behavior, i.e., $V\rho^2 \sim$ constant, following the marginal stability theory [24]. We suppose that the variation of these dimensional shape characteristics during the morphological transition is due to the competition effects between $V\lambda^2 \sim$ constant (for the shallow cells) and $V\rho^2 \sim$ constant (for the deep cells).

The curves shown above are based on averaged quantities, and from the theoretical viewpoint these selections seem to be unique ones. However, because of the constraint of the finite computational domain used here, the morphological wavelength cannot be exactly obtained. As shown in Fig. 6, because the domain size W is not integer times of λ, the simulated wavelengths for $V = 32.5$, 35, 37.5, 50, and 60 μm/s are all 50 μm, but only the one for $V = 40$ μm/s is about 60 μm. To clarify this point, the morphologies obtained from different domain sizes ($W = 300$, 400, and 500 μm) under the pulling speed of $V = 40$ μm/s are compared. The averaged wavelengths calculated are 60, 57.14, and 55.56 μm, respectively. The variation is only about 8%. In short, after these tests with different domain sizes, we can conclude that the increase in the wavelength for $V = 40$ μm/s is not caused by numerical errors.

To summarize the previous results, the detailed wavelength variations with the classic MS loop [1] are plotted in Fig. 9. As shown, with the increasing pulling speed, the transitions from a planar interface to the shallow cells of $\lambda_c/2$, finite-depth cells having a smaller wavelength, and deep cells are clearly illustrated. By using our present phase-field model, the local Gibbs–Thompson condition is satisfied quantitatively. The formation of deep cells with change of overall morphologies is also

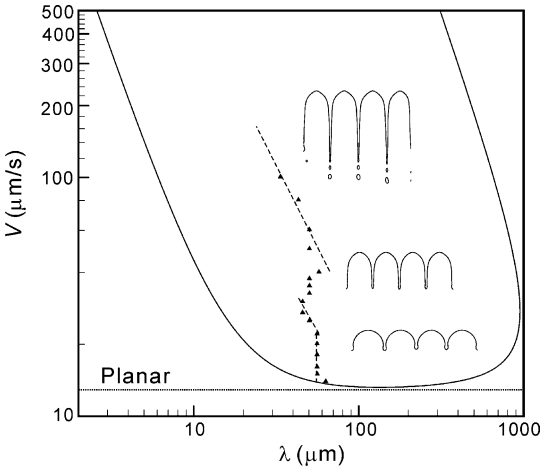

Fig. 9. Comparison of the simulated wavelengths and speeds with the classical MS loop. Morphologies of shallow cells, finite-depth cells, and deep cells are illustrated.

simulated for the first time. More importantly, the simulated results are consistent with the observed ones in the previous experiments [4,22,23]. The dramatic increase of the wavelength with the pulling speed at the transition from shallow to deep cells is found in the simulation for the first time.

3.2. Onset of initial crossover instability

When the pulling speed V in a directional solidification system exceeds the critical value V_c, the planar interface eventually destabilizes and evolves into a cellular or dendritic pattern. The WL theory [7] analyzes the morphological stability of the planar interface during the transient, and also determines a crossover time t_0 when the modulation amplitude becomes comparable to the initial instability wavelength λ_0. This wavelength is different from the onset one in the MS theory, where the wavelength appears from the planar interface at a steady-state concentration profile.

To further study the transient near the onset of the initial instability, the morphological evolution from a planar interface ($c_0 = 0.05$ mol%, $G = 100$ K/cm, $V = 50$ μm/s) is plotted in Fig. 10. As shown, at first, the planar interface breaks up at an initial instability wavelength λ_0, which is the onset of the initial instability. After the long-time scale ($\sim 5D_L/kV^2$) global coarsening and pinching-off, several tips in this array merge, and finally a steady-state wavelength λ and a deep-cellular structure are developed. In general, the initial instability wavelength λ_0 is much smaller than λ.

For comparison purposes, we have also solved numerically the equations in the WL theory [7] and the crossover time t_0 and wavelength λ_0 are verified by the results in Refs. [7,8]. Then, the crossover wavelength based on the WL theory in this study as a function of the

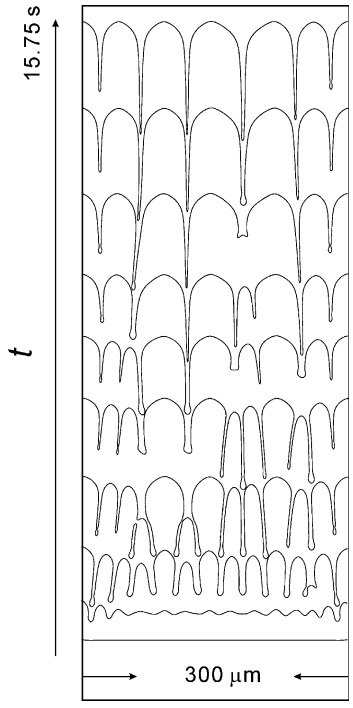

Fig. 10. Time evolution of the morphology from a planar solidification to deep cells ($c_0 = 0.05$ mol%, $G = 100$ K/cm, and $V = 50$ μm/s).

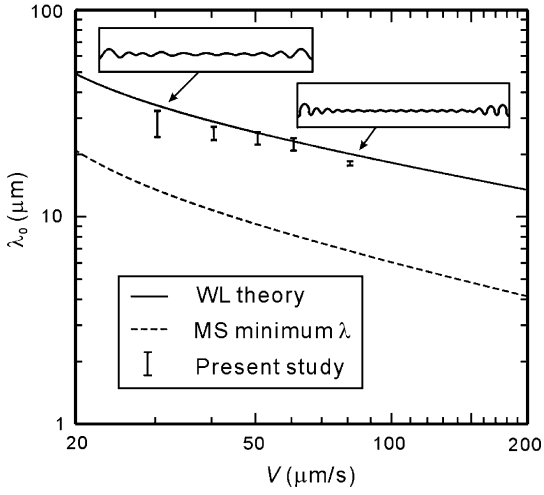

Fig. 11. Comparison of simulated crossover wavelength λ_0 with the one predicted by the WL theory; the minimum wavelength predicted by the MS theory is included for comparison.

pulling speed is further calculated. As shown in Fig. 11, the phase field simulated λ_0 is slightly smaller than the one predicted by the WL theory. The minimum wavelength at the MS loop is included for comparison. Besides, the simulated morphologies at the onset of initial instability under $V = 30$ and 80 μm/s are also highlighted. Because of the numerical noises resulting from the symmetric boundaries, the wavelength perturbation near the boundaries is slightly larger. This factor causes a small amount of non-uniformity for calculating

crossover wavelength. By taking a longer crossover time defined at the center region, the cells there will be more developed and the wavelength will be reduced slightly. Therefore, we have purposely represented our λ_0 using an error bar. In addition to the reasonable discrepancy, the overall trend is also very alike. Interestingly, the experimental results [7,25] for solidification from a flat interface also show some difference, being lower, from the ones predicted by the WL theory. We do not have a better explanation for the discrepancy. However, it should be pointed out that the amplitude equation proposed in the WL theory for determining the crossover time assumes the amplitude is about the same as the wavelength. However, such a large interface deformation is not consistent with the linear stability assumption, and this could be the major error from the analytical consideration.

4. Conclusions

With the newly proposed phase field model, we have quantitatively simulated for the first time the morphological evolution from a planar interface to deep cells during a thin-film directional solidification of an SCN/acetone alloy. With this model, a thick interface, but smaller than the tip radius, can be used without the introduction of solutal trapping. The calculated crossover wavelength λ_0 decreases with the increasing pulling speed, and shows reasonable agreement with the WL theory. The cell characteristics from shallow to deep cells are consistent with the experimental observations. In particular, before turning into deep cells, the wavelength increases with the pulling speed. This is consistent with experiments and is simulated for the first time as well. Although the present phase field simulation becomes quite efficient by using a thick interface here, the simulation from deep cells to dendrites (side branching) still remains a great challenge.

Acknowledgments

The authors are grateful for the financial support from the National Science Council of Taiwan.

References

[1] Mullins WW, Sekerka RF. J Appl Phys 1964;35:444.
[2] Lee JTC, Tsiveriotis K, Brown RA. J Cryst Growth 1992;121:536.
[3] Jackson KA, Hunt JD. Acta Metall 1965;13:1212.
[4] Eshelman MA, Seetharaman V, Trivedi R. Acta Metall 1988;36:1165.
[5] Ungar LH, Brown RA. Phys Rev B 1985;31:5931.
[6] Boettinger WJ, Coriell SR, Greer AL, Karma A, Kurz W, Rappaz M, et al. Acta Mater 2000;48:43.
[7] Warren JA, Langer JS. Phys Rev E 1993;47:2072.
[8] Losert W, Shi BQ, Cummins HZ. Proc Natl Acad Sci USA 1998;95:439.
[9] Boettinger WJ, Warren JA, Beckermann C, Karma A. Annu Rev Mater Res 2002;32:163.
[10] Wheeler AA, Boettinger WJ, McFadden GB. Phys Rev A 1992;45:7424.
[11] Provatas N, Goldenfeld N, Dantzig J. Phys Rev Lett 1998;80:3308.
[12] Ahmad NA, Wheeler AA, Boettinger WJ, McFadden GB. Phys Rev E 1998;58:3436.
[13] Karma A, Rappel WJ. Phys Rev E 1996;53:3017.
[14] Amberg G. Phys Rev Lett 2003;91:265505.
[15] Karma A. Phys Rev Lett 2001;87:115701.
[16] Lan CW, Shih CJ. Phys Rev E 2004;69:031601.
[17] Ramirez JC, Beckermann C, Karma A, Diepers H-J. Phys Rev E 2004;69:051607.
[18] Lan CW, Shih CJ. J Cryst Growth [submitted].
[19] Beckermann C, Diepers H-J, Steinbach I, Karma A, Tong X. J Comput Phys 1999;154:468.
[20] Aziz MJ, Kaplan T. Acta Metall 1988;36:2335.
[21] Lan CW, Liu CC, Hsu CM. J Comput Phys 2002;178:464.
[22] Kurowski P, de Cheveigne S, Faivre G, Guthmann C. J Phys (Paris) 1989;50:3007.
[23] Kurowski P, Guthmann C, de Cheveigne S. Phys Rev A 1990;42:7368.
[24] Oldfield W. Mater Sci Eng 1973;11:211.
[25] Trivedi R, Somboonsuk K. Acta Metall 1985;33:1061.